


Simple Method of Including Density Variation in Quantitative Continuum Phase-Change Models

M. J. Welland¹ and N. Ofori-Opoku¹

Canadian Nuclear Laboratories, Chalk River, K0J 1J0 Ontario, Canada

 (Received 16 October 2021; accepted 5 January 2022; published 15 February 2022)

We present a simple, quantitative, and thermodynamically self-consistent method of capturing density and pressure variation in continuum phase-change models. The formalism shows how the local state of homogenous dilation may be entirely given by species concentration in an Eulerian formulation. A hyperelastic contribution to the thermodynamic potential generalizes the lattice constraint while permitting composition, temperature, and phase-dependent specific volumes. We compare the results of models implementing this paradigm to those with the lattice constraint by examining the composition and size-dependent equilibrium of a Ni-Cu nanoparticle in its melt and free dendritic growth.

DOI: [10.1103/PhysRevLett.128.075701](https://doi.org/10.1103/PhysRevLett.128.075701)

Phase transitions play a critical role across a multitude of disciplines in the physical sciences from phase transitions in the early Universe [1,2], terrestrial climate models [3], to those of proteins and cell membranes in biological systems [4,5]. Numerical tools such as phase-field and moving boundary models have proven their power and versatility in the study of phase transitions, amplified by their ability to incorporate equilibrium thermodynamics [6,7]. In materials science and physics these tools robustly capture complex interface morphologies and perturbation of bulk thermodynamics by interfacial excess energy which is particularly relevant to the engineering of advanced functional materials through controlled phase segregation, e.g., in nanoparticles [8–12]. Further, they readily fit with multiphysics treatments including heat and mass transport [13,14], elasticity [15], and electrostatics [16] within a framework that permits a departure from equilibrium thermodynamics by kinetic effects during, e.g., rapid solidification [17–19].

Despite their importance, these models often ignore density variations between coexisting phases and assume all species have equivalent specific volumes [20–25]. This approximation is useful to simplify the model and its solution but is ultimately troubling since density variations during phase transition directly affect the evolution of the system. In particular at the nanoscale where the emergence of capillary pressure and elastic dilation, leading to a departure from bulk thermodynamic equilibrium, is a key phenomenon.

The purpose of this Letter is to put forth a simple formulation that accurately and quantitatively accounts for density variations and pressure changes during phase transitions in a thermodynamically self-consistent fashion. We capture density variations by relaxing the lattice constraint, the assumption of a fixed density of species, which is assumed in most descriptions, and formulating our

model in an Eulerian frame. Species concentrations expressed in the Eulerian frame are weighted by their state-dependent specific volumes, the sum of which is shown to correspond to the local state of elastic dilation and compression. The strain incurs a pressure response which effectively generalizes the lattice constraint and permits variations in density. The impact of this formulation is highlighted through comparison with other models for a Ni-Cu nanoparticle in equilibrium with its melt and free dendritic growth. A more detailed account will be provided in a companion article [26].

The Gibbs free energy of a phase, $G(n_i, P)$, is the thermodynamic potential commonly employed when discussing phase transitions, and is expressed as a function of the abundance of species i , n_i , and pressure P . Commonly, the pressure is taken as a reference pressure $P = P^0$, and its functional dependence is ignored. For the remainder of this work, quantities that assume a fixed pressure and neglect the pressure dependence are denoted by a prime, e.g., $G' = G(n_i, P = P^0)$.

When considering systems with homogenous elastic deformation, the Helmholtz energy of a phase, $A(n_i, V)$, is relevant and is normally related to G by a Legendre transform. However, since the pressure dependence of G is neglected, this transformation is incomplete. Pragmatically, one may consider G' to describe the *chemical* contribution to the energy and add a homogenous elastic strain energy function $A^{\text{el}}(n_i, V)$,

$$A(n_i, V) = G'(n_i, P^0) + A^{\text{el}}(n_i, V), \quad (1)$$

where V is the volume of the system. The system is then discretized in an Eulerian frame of reference with volume element V^0 . The Helmholtz energy density $a(c_i, \Delta) = (A/V^0)$ is then defined in terms of the concentration,

$c_i = (n_i/V^0)$, and dilation, $\Delta = (V/V^0)$, with respect to the Eulerian frame of reference.

To understand how dilation is captured in the current work, we consider the deformation of the material as a sequence of transformations from the reference to the real configuration as depicted in Fig. 1 [27]. In this figure, the material (Lagrangian) frame is represented as an array of points while the Eulerian frame is represented by a grid with a volume element V^0 . The stress-free configuration is included for generality and includes dilations that do not incur elastic strains, such as thermal expansion or piezoelectric effects but exclude, phase change.

Following multiplicative decomposition, the dilation from the reference to real configuration Δ can be decomposed into that of the reference to stress-free configuration Δ^{sf} and the stress-free to the real configuration Δ^{el} as $\Delta = \Delta^{\text{sf}} \Delta^{\text{el}}$.

The shaded region deforms from the reference configuration V^0 via a stress-free configuration V^{sf} to the real configuration V , and lends itself most readily to standard thermodynamic formulations in which the abundance and volume are separate state variables. The specific volumes are defined as $v_i = (\partial V / \partial n_i)$, such that $V = \sum_i n_i v_i$. Likewise, the stress-free volume $V^{\text{sf}} = \sum_i n_i v_i^{\text{sf}}$, and the reference volume $V^0 = \sum_i n_i v_i^0$ with specific volumes v_i^{sf} and v_i^0 defined similarly.

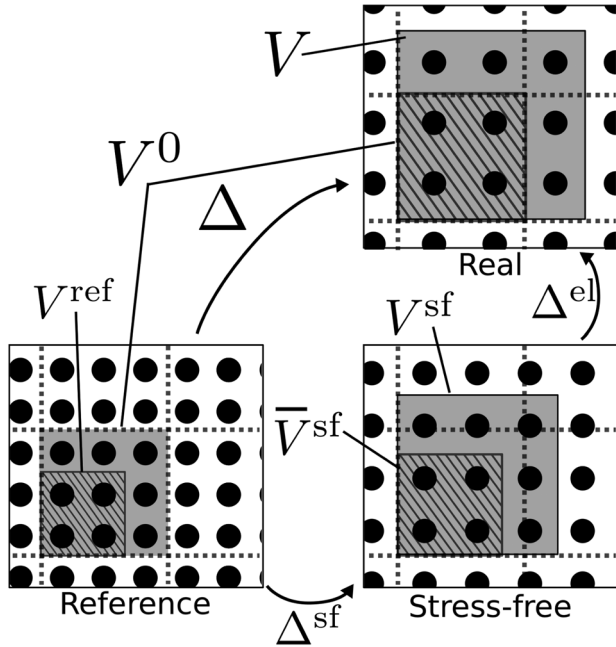


FIG. 1. The total dilation from the reference to real configurations via an intermediate stress-free configuration. The shaded region dilates from a reference volume V^0 to the final volume V while the hatched region undergoes approximately the same dilation from V^{ref} to V^0 . The abundance of particles in V^0 , which is the concentration with respect to the Eulerian frame of reference, is related to the total dilation via their specific volumes.

The same deformation transforms the hatched volume in Fig. 1 from V^{ref} via \bar{V}^{sf} to V^0 . Examining the real configuration, the hatched region contains c_i particles such that the reference volume may be approximated as $V^{\text{ref}} = \sum_i c_i v_i^0 V^0$.

Finally, if we assume that length scale of variation of the dilations to be small compared to the volume V^0 , they can be approximated as

$$\Delta = \frac{V}{V^0} = \frac{V}{\sum_i n_i v_i^0} \approx \frac{V^0}{V^{\text{ref}}} = \frac{1}{\sum_i c_i v_i^0}, \quad (2)$$

$$\Delta^{\text{el}} = \frac{V}{V^{\text{sf}}} \approx \frac{V^0}{\bar{V}^{\text{sf}}} = \frac{1}{\sum_i c_i v_i^{\text{sf}}}. \quad (3)$$

Equations (2) and (3) show how the dilation depends on the system volume and abundance in the Lagrangian frame, which is easily incorporated into typical thermodynamic treatments, but the instantaneous values may be approximated in terms of the local concentration (defined with respect to the Eulerian frame) and the specific volumes.

With this representation of dilation, a number of hyperelastic functions may be used. For the sake of discussion, we assume a neo-Hookean strain energy function expressed in the stress-free configuration $A^{\text{el}} = (V^{\text{sf}}/2)\kappa \ln^2 \Delta^{\text{el}}$, and the corresponding density

$$a^{\text{el}} = \frac{1}{\Delta^{\text{el}}} \frac{\kappa}{2} \ln^2 \Delta^{\text{el}}, \quad (4)$$

where κ is the isothermal bulk modulus. The pressure is

$$P \equiv -\frac{\partial A}{\partial V} = -\frac{\partial A^{\text{el}}}{\partial V} = -\frac{1}{\Delta^{\text{el}}} \kappa \ln \Delta^{\text{el}}. \quad (5)$$

The chemical potential follows from Eq. (1),

$$\mu_i \equiv \frac{\partial A}{\partial n_i} = \frac{\partial G'}{\partial n_i} + \frac{\partial A^{\text{el}}}{\partial n_i} = \mu'_i + P \Delta^{\text{el}} v_i^{\text{sf}} \left[1 - \frac{1}{2} \ln \Delta^{\text{el}} \right], \quad (6)$$

where $\mu'_i = (\partial G' / \partial n_i)$ is the chemical potential without pressure dependence.

From Eq. (1), we then have $a = g'(c_i) + a^{\text{el}}(c_i, \Delta^{\text{el}}) = \sum_i c_i \mu_i - \Delta P$ or explicitly in terms of prime quantities,

$$a = \sum_i c_i \mu'_i + \frac{1}{\Delta^{\text{el}}} \frac{\kappa}{2} \ln^2 \Delta^{\text{el}}. \quad (7)$$

Equation (7), along with Δ^{el} in Eq. (3) shows that the free energy density in the Eulerian frame is a function only of the concentrations in the same frame, i.e., $a(c_i, \Delta) \rightarrow a(c_i)$ since the dilation is entirely determined by the concentrations. While it may appear that this formulation involves a loss of information, the interpretation is that in the Eulerian frame movement of mass across adjacent elements

or through the boundary of the domain is a consequence of dilation rather than a change in volume in the material frame.

The grand potential density $\psi(\mu_i, \Delta)$ may be defined as the Legendre transform of a ,

$$\psi = a - \sum_i c_i \mu_i, \quad (8)$$

$$= -P\Delta. \quad (9)$$

Variation of the grand potential between phases naturally encapsulates the driving force for the phase transformation as well as excess quantities when considering equilibrium conditions. In the current model, Eq. (9) is readily evaluated from Eq. (5). Models employing the lattice constraint calculate the pressure from Eq. (8) as discussed below. However, without consideration of a volume-pressure term, Eq. (8) would normally yield zero via the Gibbs-Duhem relation if not for quadratic approximations or the imposition of the lattice constraint, and therefore its use may be errant as discussed further in [26].

We now demonstrate this formulation for a quintessential mesoscale phase-change problem of solidification where we consider the equilibrium of a nanoparticle with radius r in equilibrium with its melt. Equilibrium is described by the Young-Laplace relation, $P_r^s - P^l = (2\sigma/r)$, where σ is the interfacial energy, such that as $r \rightarrow \infty$ the flat interface bulk equilibrium is approached with $P_{r \rightarrow \infty}^s = P^l$.

If we consider fixed composition in the solid phase, such as a stoichiometric solid, Thomson's equation $\mu_{i,r} - \mu_{i,\infty} \approx v_i(2\sigma/r)$ [28] is readily recovered from Eq. (6) via the reasonable assumption that $v_i \approx \Delta^{\text{el}} v_i^{\text{sf}}$ and assuming infinitesimal elastic dilation, $\Delta^{\text{el}} \rightarrow 1$. The term $[1 - \frac{1}{2} \ln \Delta^{\text{el}}]$, therefore modifies this relationship in the general case of compressible materials.

To aid in the comparison of models, dilation is assumed infinitesimal, all specific volumes are equal, and mass transport is assumed to be quasistatic. Simulations assume spherical symmetry and are in 1D. This scenario is contrived to correspond to the discussion found in Chap. 6.6 of [29].

The importance of the current formulation is demonstrated in comparison with models derived using the lattice constraint through a sharp interface model with dynamic variables c_i and three phase-field grand potential implementations with dynamic variable(s) μ_i : (i) Model A - A sharp interface model with the current formulation was solved with the aid of a Lagrange multiplier to constrain the chemical equilibrium. (ii) Model B - A phase-field model with quadraticized potential of the current work and two explicit components. (iii) Model C - A phase-field model with quadraticized grand potential with one component and using the lattice constraint. (iv) Model D - A phase-field model with an analytical grand potential using the lattice constraint.

Details of the implementations are provided in [26], in which it is noted that this work is a generalization of the Stefan sharp interface model based on the thermodynamic driving force.

Unlike conventional formulations, the current formulation allows the individual chemical potentials and the phase-specific pressures to be calculated directly. As a result, it is possible to specify the liquid pressure in models A and B, whereas models C and D only allow differences in pressure to be considered.

We choose the Ni-Cu system at 1400 K with the Gibbs free energies densities for the liquid and solid defined as

$$g^{l,s}(c_{\text{Ni}}, c_{\text{Cu}}) = x_{\text{Ni}} g_{\text{Ni}}^0 + x_{\text{Cu}}^s g_{\text{Cu}}^0 + \frac{RT}{v_m} [x_{\text{Ni}} \ln x_{\text{Ni}} + x_{\text{Cu}} \ln x_{\text{Cu}}], \quad (10)$$

$$g^{l,l}(c_{\text{Ni}}, c_{\text{Cu}}) = \frac{RT}{v_m} [x_{\text{Ni}} \ln x_{\text{Ni}} + x_{\text{Cu}} \ln x_{\text{Cu}}], \quad (11)$$

where the mole fractions $x_{\text{Ni}} = [c_{\text{Ni}}/(c_{\text{Ni}} + c_{\text{Cu}})]$ and $x_{\text{Cu}} = [c_{\text{Cu}}/(c_{\text{Ni}} + c_{\text{Cu}})]$, and $g_{\text{Ni}}^0 = L_{\text{Ni}}[(T - T_{\text{Ni}}^m)/T_{\text{Ni}}^m]$, and $g_{\text{Cu}}^0 = L_{\text{Cu}}[(T - T_{\text{Cu}}^m)/T_{\text{Cu}}^m]$. The Helmholtz energy densities follow from Eq. (7) with (3). The material properties are defined in Table 1. For this demonstration, all $v_i^s = v_m$, an average specific volume constant between phases useful for comparison with lattice-constraint models. For the subsequent dendrite example below, the listed v_i^s will be used.

For model A, the interface is placed in a domain with a shared boundary at the position z_{int} . This shared boundary is constrained by equal flux conditions $J_i^s = J_i^l$ and local equilibrium conditions through the expression of equal chemical potentials enforced through a Lagrange multiplier. The velocity of z_{int} is determined by the rate equations,

TABLE I. Parameters for the Ni-Cu system demonstrative model from [20,30,31] at 1400 K. Bulk moduli are representative. v_m is an average specific volume useful for comparison between models.

Symbol	Value	Unit
g_{Ni}^0	-446.06	J cm ⁻³
g_{Cu}^0	54.06	J cm ⁻³
σ	1	J cm ⁻²
κ^s	100	GPa
κ^l	1	GPa
v_m	7.42	cm ³ mol ⁻¹
v_{Cu}^s	7.72	cm ³ mol ⁻¹
v_{Cu}^l	8.11	cm ³ mol ⁻¹
v_{Ni}^s	6.99	cm ³ mol ⁻¹
v_{Ni}^l	7.29	cm ³ mol ⁻¹

$$\frac{\partial z_{\text{int}}}{\partial t} = M_\phi \left[\psi^l - \psi^s \frac{2\sigma}{r} \right], \quad (12)$$

$$0 = \nabla \cdot \nabla \mu_i, \quad (13)$$

where ψ^π is calculated with Eq. (5). Additionally, $P^l = 0$ is imposed as a Dirichlet boundary condition.

The equations for the grand potential phase-field models are

$$\frac{\partial \phi}{\partial t} = \sigma \left(6d\nabla^2 \phi - \frac{3}{d} \frac{\partial \phi^2 [1 - \phi]^2}{\partial \phi} \right) - [\psi^s - \psi^l] \frac{\partial p}{\partial \phi}, \quad (14)$$

$$\frac{\partial c_i}{\partial \phi} \frac{\partial \phi}{\partial t} = \nabla \cdot \nabla \mu_i, \quad (15)$$

where d is the interface width and $p = \phi^3(10 - 15\phi - 6\phi^2)$.

The differences in phase-field implementations emerge from the definitions and expressions for ψ . Model *B* uses a quadraticized version of the formulation presented here and takes the form $\psi^\pi - \psi^* = -\kappa^\pi \sum_i (\partial c_i^\pi / \partial \mu_i) [\mu_j - \mu_j^*]$, where the asterisk signifies the expansion point and $\pi = s, l$. Model *C* utilizes a generalized grand potential in two components and is quadraticized such that $\psi^\pi - \psi^* = -\frac{1}{2} \sum_i [\mu_i - \mu_i^*] [c_i^\pi + c_i^{\pi*}]$. Model *D* corresponds to the lattice constrained formulation with $c \equiv c_{\text{Ni}} = 1 - c_{\text{Cu}}$ and $\psi^s = g_{\text{Cu}}^0 + \ln\{1 - (1/[1 + \exp(g_{\text{Ni}}^0 - g_{\text{Cu}}^0 - \mu_i)])\}$.

The shift in solubility may be calculated analytically through the lowest common tangent construction. Since all species are assumed to have the same specific volume, pressurization of the solid results in the verticle displacement of g^s by P^s [29]. The maximal pressure difference is calculated as $\Delta P^{\text{max}} = g^s(x_{\text{Ni}} \rightarrow 1) - g^l(x_{\text{Ni}} \rightarrow 1) = g_{\text{Cu}}^0 = 0.446$ GPa, which corresponds to a nanoparticle of radius 4.484 nm.

The solidus and liquidus lines for Ni are plotted as a function of $\Delta P = P^s - P^l$, along with the interdiffusion potential, $\Delta\mu = \mu_{\text{Ni}} - \mu_{\text{Cu}}$, in Fig. 2 from the analytical and simulation results.

Figure 2 shows that models *A* and *D* are in agreement with the analytical model including the logarithmic behavior of the chemical potential with mole fraction. Models *B* and *C* show roughly linear trends for all quantities following a slight curvature in model *B* at small ΔP . Furthermore, whereas model *C* follows $\Delta\mu$ over a large range of pressures but underpredicts the solubility curves, model *B* brackets the solubility curves but deviates from $\Delta\mu$. Neither *B* nor *C* predicts the upturn in $\Delta\mu$ at higher ΔP as this is due to the asymptotic logarithmic behavior which both quadraticized potentials neglect.

In all simulations, the dependence of ΔP on particle radius (not shown), reproduces the Young Laplace equation within numerical accuracy. Models *A* and *B* however, also permit imposing the liquid absolute pressure $P^l = 0$.

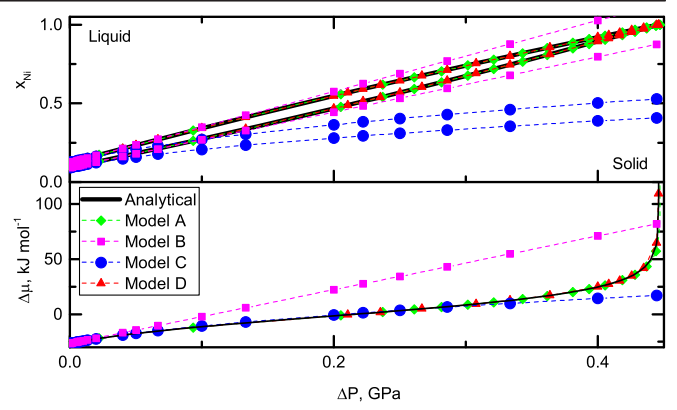


FIG. 2. Comparison of simulation results of solidus and liquidus (above) and interdiffusion potential (below) at the interface, plotted along with the analytical solution with models identified in the text.

Meanwhile, the pressurized solid compresses as shown in Fig. 3 as total concentration in the solid phase exceeds unity, reflecting elastic compression in accordance with Eq. (5).

Models *C* and *D* determine the pressure to be the grand potential per Eq. (8) and leads to a correct prediction for ΔP , without the ability to control the pressure in either phase explicitly. This explains the wide use of the lattice constrained model in cases where the absolute pressure is not important and where specific volumes are all equal.

We now explore the impact of composition and phase-dependent specific volumes using model *B* with v_i^π in Table I. We simulate dendritic growth for three different supersaturations, $\Omega = [(c_i^{\text{avg}} - c_i^{l*}) / (c_i^{s*} - c_i^{l*})]$, initialized with a circular seed of radius $r = 200$ nm with the liquid beginning at $\sim c_i^{\text{avg}}$. As is standard, the model is made anisotropic by including an order parameter dependence in the surface energy gradient term [32]. We consider only a quarter of the growing system due to the fourfold symmetry of the growing crystal in 2D and restrict our data analysis to

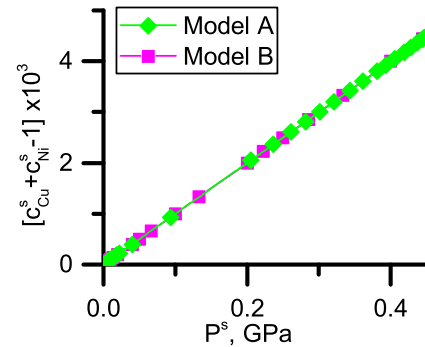


FIG. 3. Solid-phase concentrations with P^s predicted from models *A* and *B* based on the current work showing the total concentration in the solid phase exceeds 1, reflecting elastic compression linearly related to the pressure described by Eq. (5).

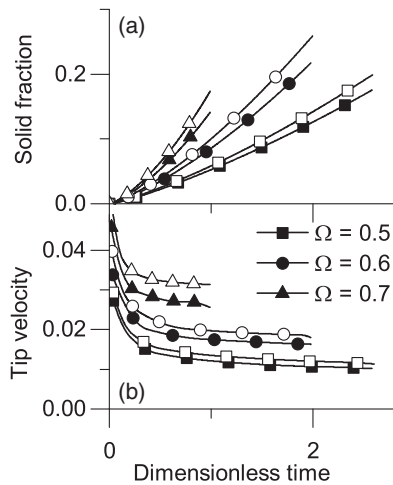


FIG. 4. Comparison of (a) solidification fraction and (b) dendrite tip velocity for three supersaturations vs dimensionless time. Data series are truncated when the tip velocity departs from the steady-state regime. Filled and empty symbols correspond to a constant $v_i^\pi = v_m$ and variation between phase and species listed in Table I, respectively.

the portion of the simulation during the initialization and free growth steady-state regime. Further details are presented in [26].

Two measures of the growth rate, the change in solid fraction and the dendrite tip velocity, are shown in Fig. 4 for different supersaturations. The solid fraction is plotted in Fig. 4(a), and while larger supersaturations, i.e., larger driving forces, would intuitively lead to faster growth rates, we also observe faster growth rates in the case of variable specific volumes. This is a combination of the variable specific volumes amplifying the driving force and causing a shape-change in the growing crystal which allows it to realize faster growth rates.

The dendrite tip velocity is shown in Fig. 4(b). Consistent with the results of the solid fraction data above, we observe larger steady-state velocities during free growth in the cases of variable specific volume. Moreover, we observe that increasing supersaturation leads to a greater increase in the tip velocity when variable specific volumes are considered. Taken with the solid fraction growth in Fig. 4(a), it is likely that the shape of the dendrite is being affected by the inclusion of specific volumes as is expected considering the Young-Laplace and Thomson equations above. Presentation of the dendrite shape evolution and microsegregation [33] is presented in [26].

In summary, it is shown that through a proper description of Helmholtz potential and considering all species compositions in an Eulerian frame of reference, one may capture densification and homogenous elastic stresses in continuum-scale phase-change models robustly. Furthermore, composition and phase-dependent specific volumes are included naturally. Comparison of the current work with formulations that rely on the lattice constraint demonstrates

that while both formulations predict the interdiffusion potential and variation in pressure in accordance with classical theory, the current work additionally directly determines the individual quantities and provides a means for user imposed controls, e.g., the direct control of the pressure of a surrounding phase. Although derived for isothermal systems, extension to temperature dependence is straightforward, facilitated by the stress-free configuration. The emergence of homogenous dilation and pressure, which employs techniques from Finite Strain theory, may form a natural point of intersection with elastic and viscoplastic treatments and predict, e.g., strain and shear driven transformations and capture the structural effects of phase change, e.g., in laser-heated experiments on nuclear materials [34] and melt-processed additive manufacturing [35–37].

The research was funded by Atomic Energy of Canada Limited, under the auspices of the Federal Nuclear Science and Technology Program.

*Michael.Welland@cnl.ca

- [1] D. Boyanovsky, H. j. de Vega, and D. j. Schwarz, Phase transitions in the early and present universe, *Annu. Rev. Nucl. Part. Sci.* **56**, 441 (2006).
- [2] K. R. Dienes, J. Kost, and B. Thomas, A tale of two timescales: Mixing, mass generation, and phase transitions in the early universe, *Phys. Rev. D* **93**, 043540 (2016).
- [3] L. I. Rubinstein, *The Stefan Problem* (American Mathematical Society, Providence, Rhode Island, 1971).
- [4] G. R. Lázaro, I. Pagonabarraga, and A. Hernández-Machado, Phase-field theories for mathematical modeling of biological membranes, *Chem. Phys. Lipids* **185**, 46 (2015).
- [5] P. Mohammadi, A. S. Aranko, L. Lemetti, Z. Cenev, Q. Zhou, S. Virtanen, C. P. Landowski, M. Penttilä, W. J. Fischer, W. Wagermaier, and M. B. Linder, Phase transitions as intermediate steps in the formation of molecularly engineered protein fibers, *Commun. Biol.* **1**, 86 (2018).
- [6] M. J. Welland, Introduction to the phase-field modelling technique: A primer on the Allen-Cahn and Cahn-Hilliard models, in *OECD NEA: State-of-the-Art Report on Multi-Scale Modelling Methods* (Organization for Economic Cooperation and Development, Boulogne-Billancourt, 2020), pp. 128–142, https://www.oecd-nea.org/jcms/pl_46415/state-of-the-art-report-on-multi-scale-modelling-methods.
- [7] M. J. Welland, B. J. Lewis, and W. T. Thompson, A comparison of Stefan and phase field modeling techniques for the simulation of melting nuclear fuel, *J. Nucl. Mater.* **376**, 229 (2008).
- [8] M. J. Welland, D. Karpeyev, D. T. O'Connor, and O. Heinonen, Miscibility gap closure, interface morphology, and phase microstructure of 3D Li_xFePO_4 nanoparticles from surface wetting and coherency strain, *ACS Nano* **9**, 9757 (2015).
- [9] A. Ulvestad, M. J. Welland, W. Cha, Y. Liu, J. W. Kim, R. Harder, E. Maxey, J. N. Clark, M. J. Highland, H. You, P. Zapol, S. O. Hruszkewycz, and G. B. Stephenson,

- Three-dimensional imaging of dislocation dynamics during the hydriding phase transformation, *Nat. Mater.* **16**, 565 (2017).
- [10] A. Ulvestad, M. J. Welland, S. S. E. Collins, R. Harder, E. Maxey, J. Wingert, A. Singer, S. Hy, P. Mulvaney, P. Zapol, and O. G. Shpyrko, Avalanching strain dynamics during the hydriding phase transformation in individual palladium nanoparticles, *Nat. Commun.* **6**, 10092 (2015).
- [11] I. Steinbach, Phase-field model for microstructure evolution at the mesoscopic scale, *Annu. Rev. Mater. Res.* **43**, 89 (2013).
- [12] B. Nestler, H. Garcke, and B. Stinner, Multicomponent alloy solidification: Phase-field modeling and simulations, *Phys. Rev. E* **71**, 041609 (2005).
- [13] M. J. Welland, E. Tenuta, and A. A. Prudil, Linearization-based method for solving a multicomponent diffusion phase-field model with arbitrary solution thermodynamics, *Phys. Rev. E* **95**, 063312 (2017).
- [14] M. J. Welland, W. T. Thompson, B. J. Lewis, and D. Manara, Computer simulations of non-congruent melting of hyperstoichiometric uranium dioxide, *J. Nucl. Mater.* **385**, 358 (2009).
- [15] M. J. Welland and S. M. Hanlon, Prediction of the zirconium hydride precipitation barrier with an anisotropic 3D phase-field model incorporating bulk thermodynamics and elasticity, *Comput. Mater. Sci.* **171**, 109266 (2020).
- [16] J. Guyer, W. Boettinger, J. Warren, and G. McFadden, Model of electrochemical “double layer” using the phase field method, *Phys. Rev. E* **69**, 021603 (2004).
- [17] P. K. Galenko and D. A. Danilov, Model for free dendritic alloy growth under interfacial and bulk phase nonequilibrium conditions, *J. Cryst. Growth* **197**, 992 (1999).
- [18] A. A. Wheeler, W. J. Boettinger, and G. B. McFadden, Phase-field model of solute trapping during solidification, *Phys. Rev. E* **47**, 1893 (1993).
- [19] M. J. Welland, D. Wolf, and J. E. Guyer, Multicomponent phase-field model for extremely large partition coefficients, *Phys. Rev. E* **89**, 012409 (2014).
- [20] J. A. Warren and W. J. Boettinger, Prediction of dendritic growth and microsegregation patterns in a binary alloy using the phase-field method, *Acta Metall. Mater.* **43**, 689 (1995).
- [21] M. Plapp, Unified derivation of phase-field models for alloy solidification from a grand-potential functional, *Phys. Rev. E* **84**, 031601 (2011).
- [22] A. Karma, Phase-Field Formulation for Quantitative Modeling of Alloy Solidification, *Phys. Rev. Lett.* **87**, 115701 (2001).
- [23] B. Echebarria, R. Folch, A. Karma, and M. Plapp, Quantitative phase-field model of alloy solidification, *Phys. Rev. E* **70**, 061604 (2004).
- [24] S. G. Kim, A phase-field model with antitrapping current for multicomponent alloys with arbitrary thermodynamic properties, *Acta Mater.* **55**, 4391 (2007).
- [25] C. Tong, M. Greenwood, and N. Provatas, Quantitative phase-field modeling of solidification in binary alloys with nonlinear phase coexistence curves, *Phys. Rev. B* **77**, 064112 (2008).
- [26] M. J. Welland and N. Ofori-Opoku, Introducing density variation and pressure in thermodynamically self-consistent continuum phase-change models including phase-field, *Phys. Rev. Mater.* (to be published).
- [27] V. A. Lubarda, Constitutive theories based on the multiplicative decomposition of deformation gradient: Thermoelasticity, elastoplasticity, and biomechanics, *Appl. Mech. Rev.* **57**, 95 (2004).
- [28] C. H. P. Lupis, *Chemical Thermodynamics of Materials* (North-Holland, New York, 1983).
- [29] M. Hillert, *Phase Equilibria, Phase Diagrams and Phase Transformations: Their Thermodynamic Basis*, 2nd ed. (Cambridge University Press, Cambridge, 2007).
- [30] R. N. Abdullaev, Yu. M. Kozlovskii, R. A. Khairulin, and S. V. Stankus, Density and thermal expansion of high purity nickel over the temperature range from 150 K to 2030 K, *Int. J. Thermophys.* **36**, 603 (2015).
- [31] M. M. Demin, O. N. Koroleva, A. A. Aleksashkina, and V. I. Mazhukin, Molecular-dynamic modeling of thermophysical properties of phonon subsystem of copper in wide temperature range, *Math. Mon.* **47**, 137 (2020).
- [32] N. Ofori-Opoku and N. Provatas, A quantitative multi-phase field model of polycrystalline alloy solidification, *Acta Mater.* **58**, 2155 (2010).
- [33] D. A. Kessler, J. Koplik, and H. Levine, Pattern selection in fingered growth phenomena, *Adv. Phys.* **37**, 255 (1988).
- [34] M. J. Welland, The effect of structural mechanics on the simulation of melting nuclear fuel, *International Youth in Nuclear Generation Bulletin* (2011), pp. 53–64, https://issuu.com/iync/docs/iync_buletin_spring11_n1.
- [35] S. Ghosh, L. Ma, N. Ofori-Opoku, and J. E. Guyer, On the primary spacing and microsegregation of cellular dendrites in laser deposited Ni-Nb alloys, *Model. Simul. Mater. Sci. Eng.* **25**, 065002 (2017).
- [36] S. Ghosh, N. Ofori-Opoku, and J. E. Guyer, Simulation and analysis of γ -Ni cellular growth during laser powder deposition of Ni-based superalloys, *Comput. Mater. Sci.* **144**, 256 (2018).
- [37] H. Azizi, A. Ebrahimi, N. Ofori-Opoku, M. Greenwood, N. Provatas, and M. Mohammadi, Characterizing the microstructural effect of build direction during solidification of laser-powder bed fusion of Al-Si alloys in the dilute limit: A phase-field study, *Acta Mater.* **214**, 116983 (2021).